# Kinetic modeling of methylene blue photodegradation by graphene/CoZnAl-MMO/TiO$_2$ as a new visible light photocatalyst

## Mina Sharifi-Bonab, Soheil Aber*, Dariush Salari

*Department of Applied Chemistry, Faculty of Chemistry, University of Tabriz, Tabriz, Iran, Tel. +98 (41) 3339 3153;*
*Fax: +98 (41) 3334 0191; emails: soheil_aber@yahoo.com/s_aber@tabrizu.ac.ir (S. Aber), sharifi8288@yahoo.com (M. Sharifi-Bonab),*
*salari@tabrizu.ac.ir (D. Salari)*

**ABSTRACT**

In this work, the kinetic modeling of methylene blue (MB) photocatalytic degradation was performed using graphene/CoZnAl-MMO/TiO$_2$ as a new photocatalyst. First, CoZnAl-LDH/GO was synthesized. It was calcined and dispersed in dimethylformamide (DMF) and was then mixed with a dispersion of TiO$_2$ in water, resulting in an active visible light photocatalyst with a band gap of 2.7 eV. The effect of the operating parameters such as pH, initial concentration of the dye solution, and the amount of the photocatalyst was investigated. The new kinetic model was written based on the basic photocatalytic degradation reaction equations. Finally, the model-predicted results were compared with the experimental ones. The validity of the proposed model was confirmed by the correlation coefficient ($R^2$ = 0.9907), the sum of squared error (SSE = 2.36 × 10$^{-5}$), and root mean square error (RMSE = 1.086 × 10$^{-3}$).

*Keywords:* Nanocomposite; Photocatalytic degradation; Titanium dioxide; Mixed metal oxide; Layered double hydroxide

## 1. Introduction

Employing photocatalysts for the elimination of water pollution under solar irradiation is a trending topic since solar irradiation is a free and abundant energy source. Conventional photocatalysts, for example, TiO$_2$ and ZnO, are active only in the UV region due to their wide band gap, which is not favorable in terms of environmental issues and operational costs. For this reason, the synthesis and application of new visible-light-active photocatalysts are essential. Metal oxides, sulfides, nitrides, and mixed metal oxides have been utilized for this purpose [1,2]. The use of TiO$_2$ as a photocatalyst is welcomed for its structural stability, non-toxicity, low cost, and high performance [3]. The photocatalytic efficiency of TiO$_2$ is promoted via reducing the band gap and electron-hole recombination rate. The doping of metals and non-metallic elements on TiO$_2$ and the preparation of its composite compounds are usually used for this purpose [4,5]. Carbon nanotubes, graphene, and layered double hydroxides (LDHs) are the porous materials used to produce photocatalytic composites.

Due to plate structure, high surface area, having functional groups, and the possibility of electron resonance in their structure, graphene oxide (GO) and graphene are used to prepare photocatalytic composite compounds. They also inhibit the agglomeration of the photocatalyst and the electron-hole recombination [6].

LDHs have a layered structure of divalent and trivalent metal hydroxides with interlayer anions. They have a general formula as follows [7]:

$$\left[ M_{(1-x)}^{2+} M_x^{3+} \left( OH^- \right)_2 \right]^{x+} A_{\frac{x}{n}}^{n-} \cdot m H_2O \tag{I}$$

---
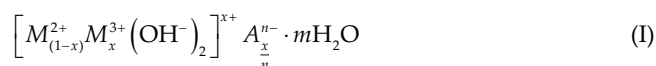
* Corresponding author.

with $M^{2+}$, $M^{3+}$, and $A^{n-}_{x/n}$ as divalent cation, trivalent cation, and interlayer anion, respectively. LDHs have found many applications in the adsorption of water pollutants [8], photocatalysis [9], and the improvement of electrode surfaces [10] due to their unique properties, including the layered structure with positively charged layers, interlayer exchangeable anions, interlayer anion variation, high surface area, electrochemical activity, and the convenient and inexpensive synthesis [11].

Oxide-based semiconductors derived from the calcination of LDHs are promising compounds for water decomposition, $CO_2$ reduction, solar cells, and the application as antibacterials and antifungals [12]. Coupling the semiconductors with matched conduction and valence bands' energy levels decreases electron-hole recombination, reduces the band gap, and consequently, leads to an increased photocatalytic activity.

There are some reports on the application of $TiO_2$ composites with LDHs, or with the mixed metal oxides (MMOs) derived from LDHs' calcination [13]. For example, the photocatalytic degradation of orange II and 4-chlorophenol by $TiO_2/Mg_2Al_{1.5}$-LDH nanocomposite under UV irradiation has been reported [13] where the presence of $Mg_2Al_{1.5}$-LDH in the composite structure reduced the $TiO_2$ agglomeration and thereby increased photocatalytic efficiency. The separation of the nanocomposite after the photocatalytic process was much easier compared with pure $TiO_2$. Kumar et al. [14] studied $CO_2$ photocatalytic reduction using $TiO_2/CoAl$-LDH nanocomposite under xenon lamp irradiation which showed more than 90% activity and selectivity for the conversion of water-soluble $CO_2$ to CO. They concluded that the presence of CoAl-LDH in the nanocomposite structure increased the $CO_2$ availability at the photocatalyst surface.

The introduction and modeling of the photocatalytic properties of MMO composites is a new topic. The first purpose of this study was to introduce a new nanocomposite MMO photocatalyst (graphene/CoZnAl-MMO/$TiO_2$), which is derived from LDH compounds and is active under visible light. The second and more important goal was the kinetic modeling of methylene blue (MB) degradation by the synthesized photocatalyst. MB was used here as a model organic pollutant. The effect of different operational parameters including pH, initial dye concentration, and catalyst content on MB removal efficiency was studied and the validity of the proposed model was examined via the comparison of experimental results with those obtained from the model.

## 2. Materials and methods

### 2.1. Materials

$TiO_2$-P25 with an average size of 25 nm was purchased from the Evonik Degussa GmbH Company. $ZnCl_2 \cdot 6H_2O$, $CoCl_2 \cdot 6H_2O$, $AlCl_3 \cdot 6H_2O$, $H_2SO_4$, $H_2O_2$, $KMnO_4$, and NaOH were obtained from the Merck Company. Graphite and methylene blue were purchased from the local market. MB characteristics are presented in Table 1. The pH value was adjusted using 0.1 M HCl and NaOH solutions. All chemicals were used directly without further purification. Distilled water was used in all steps.

### 2.2. Preparation of graphene/CoZnAl-MMO/$TiO_2$ nanocomposite

Initially, CoZnAl-LDH was prepared by the coprecipitation method. $CoCl_2 \cdot 6H_2O$, $ZnCl_2 \cdot 6H_2O$, and $AlCl_3$ were dissolved in a flask containing 40 mL of water to obtain a Co/Zn/Al molar ratio of 1:1:1. While stirring, the pH was adjusted to 10 by the NaOH solution (3 M). The achieved precipitate was aged at 60°C for 24 h, then centrifuged, washed with water, and then dried at 40°C.

The modified Hummers method was used to synthesize GO [16]. In a nutshell, 0.5 g of graphite and 0.25 g of $NaNO_3$ were mixed in 13 ml of $H_2SO_4$ in a flask which was put in an ice bath and was stirred for 1 h. Then 1.5 g $KMnO_4$ was slowly added to the contents of the flask. The contents of the flask were stirred at room temperature overnight. In the next step, 35 mL of $H_2O$ and 6 ml of $H_2O_2$ 30% were added to the above-mentioned solution and the temperature was raised to 98°C. Finally, the precipitate was washed with 5% HCl solution and then, distilled water for several times. Washing the precipitate continued until the eluent was neutral. The GO precipitate was then dried at $P$ = 0.02 mbar, $T$ = –70°C during 24 h by a freeze-dryer (Christ Alpha, 1-4LDplus, Germany).
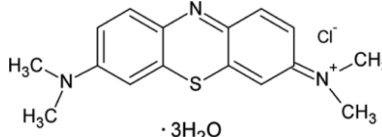
To prepare the CoZnAl-LDH/GO nanocomposite, mixtures of 0.005 g GO in 10 mL $H_2O$ and 0.1 g CoZnAl-LDH in 50 mL DMF underwent ultrasound (Parsonic, 2600s-50 W, Iran) for 40 min in separate containers. Then, the contents of these containers were mixed and stirred for 4 h at 60°C. Following that, the nanocomposite was centrifuged and washed with ethanol and dried at 40°C. To prepare the graphene/CoZnAl MMO, the prepared composite was calcined at 300°C for 12 h.

Finally, to prepare the graphene/CoZnAl-MMO/$TiO_2$ nanocomposite, the solutions of 0.15 g $TiO_2$ in 20 ml water and 0.05 g graphene/CoZnAl-MMO in 50 mL DMF underwent ultrasound for 40 min. Then the two solutions were mixed together and were then subjected to reflux for 24 h at 90°C. Finally, the nanocomposite was centrifuged, washed once with ethanol and once with water, and dried at 40°C. The pH of zero point of charge ($pH_{zpc}$) of the sample was determined in accordance with the method described in the previous work [15].

### 2.3. Characterization

Powder X-ray diffraction patterns were obtained by a Bruker Axs (Germany) model D8 advanced diffractometer using Cu $k_\alpha$ radiation ($\lambda$ = 1.54Å). The morphology of

Table 1
Characteristics of methylene blue [15]

| Structure |  |
|---|---|
| Chemical formula | $C_{16}H_{18}N_3SCl$ |
| Chemical class | Cationic dye |
| $\lambda_{max}$ (nm) | 660 |

the sample was investigated by a field emission scanning electron microscopy (FESEM) device, model ULTRA55, Carl Zeiss MST AG, (Germany). DRS curves were recorded using a T80+ UV/VIS Spectrometer PG Instruments Ltd (UK). The absorbance values of the MB solutions were measured against water at 660 nm using the same spectrophotometer.

## 2.4. Photodegradation experiments

To explore the photodegradation efficiency of the as-prepared graphene/CoZnAl-MMO/TiO$_2$ nanocomposite, the degradation of MB was examined in a photoreactor equipped with a LED lamp (10 W, Tanus, P.R.C, with white visible irradiation and no UV light) which was 2 cm above the solution surface. Both the adsorption (in the dark) and photodegradation (under irradiation) experiments were carried out simultaneously. The difference between the removal percentages of adsorption and photodegradation experiments indicated the dye removal percentage by photodegradation. All experiments were performed under batch conditions at room temperature. In a typical experiment, 0.02 g nanocomposite was added to 50 mL MB solution, while the solution was stirred by a magnetic stirrer (Germany, 814-DL, Labinco). The solution was sampled at specific intervals and the absorbance of the samples was measured using the UV-Vis spectrophotometer after centrifuging the samples. To determine the effect of the initial pH of the dye solution, a series of experiments were carried out using MB solutions (5 mg/L) with pH values of 4–9. To study the effect of initial MB and nanocomposite concentrations, similar experiments were conducted by changing their values. The obtained experimental data were used to analyze the effect of operating parameters on MB removal efficiency and also to study the photodegradation kinetic model.

The removal efficiency of the MB is expressed as:

$$R = \frac{C_0 - C_t}{C_0} \times 100 \tag{1}$$

where $C_0$ (mg/L) and $C_t$ (mg/L) are the initial and final concentrations of MB, respectively. All experiments were repeated twice, and the error bar was plotted based on the standard deviation values. The Solver tool in Microsoft Excel 2013 was used to solve the equations.

## 3. Results and discussion

### 3.1. Structural characterization

The XRD patterns of GO, TiO$_2$-P25, CoZnAl-LDH, and graphene/CoZnAl-MMO/TiO$_2$ are shown in Fig. 1. Graphene oxide exhibited its characteristic peak at 2θ = 12.15° (JCPDS No. 41-1487) [17]. CoZnAl-LDH adequately shows the characteristic peaks of the LDHs family. Peaks observed at 2θ = 11.8°, 23.5°, and 35°, and the dual-peak at around 61° are related to (003), (006), (110), (113) plans (JCPDS No. 15-0087) of LDH compounds, respectively [18]. According to diffraction peaks, the cell parameters were obtained as follows: $a$ = 0.994 nm, $b$ = 0.573 nm, $c$ = 1.594 nm, and the basal spacing was 0.78 nm. The disappearance of GO and LDH peaks in the graphene/CoZnAl-MMO/TiO$_2$ nanocomposite proves that after the calcination of CoZnAl-LDH/GO at 300°C, CoZnAl-LDH has completely collapsed and graphene oxide has been reduced to graphene [19]. According to the literature [19], the characteristic peak of graphene is around 24° (JCPDS No. 75-1621) [20], which overlapped with the TiO$_2$ peak in the XRD pattern of the nanocomposite. Due to the low temperature of calcination (300°C) and subsequently, the low crystallinity, the related peaks of cobalt and aluminum oxides were not observed. Such results have already been reported in the literature [21].

The DRS spectra of TiO$_2$, calcined CoZnAl-LDH/GO, and graphene/CoZnAl MMO/TiO$_2$ are shown in Fig. 2. To calculate the optical band gap, the Davis and Mott model [22] was used [Eq. (2)].

$$ah\upsilon = (h\upsilon - E_g)^n \tag{2}$$

where $a$ is the absorbance, $h\upsilon$ is the photon energy, $E_g$ is the optical band gap, and $n$ = 1/2 for allowed direct transition.

Fig. 3 shows the estimated band gap values. The band gap energies of the samples were determined by extrapolating the linear part of the $(ah\upsilon)^2$ curve against $h\upsilon$. As shown in Fig. 3, a value of 3.1 eV was obtained for the TiO$_2$ band gap. The band gaps of calcined CoZnAl-LDH/
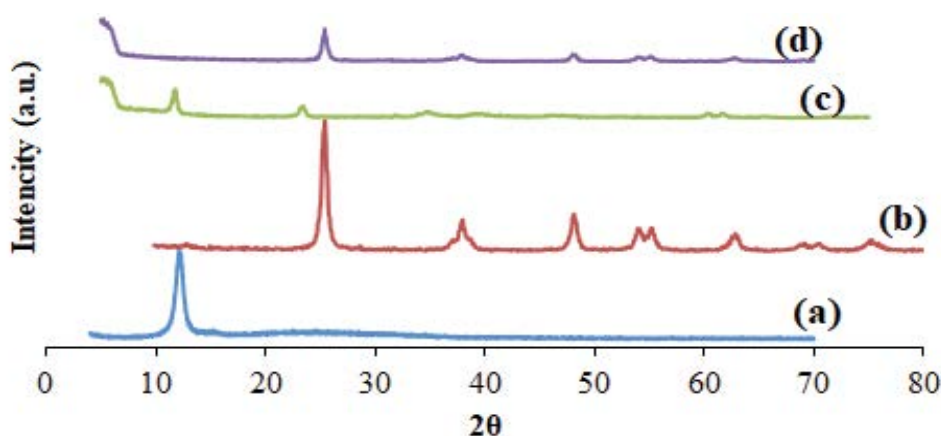


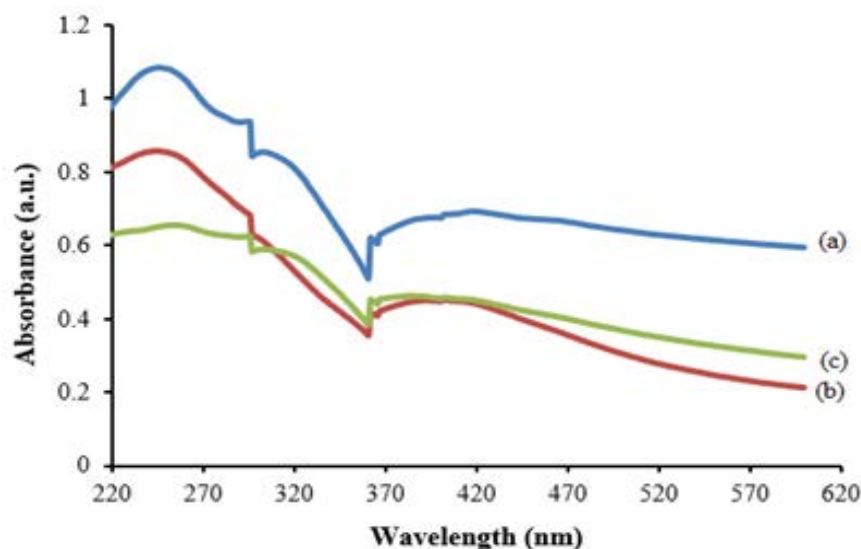Fig. 1. XRD patterns of (a) GO, (b) TiO$_2$-P25, (c) CoZnAl-LDH, and (d) graphene/CoZnAl-MMO/TiO$_2$.

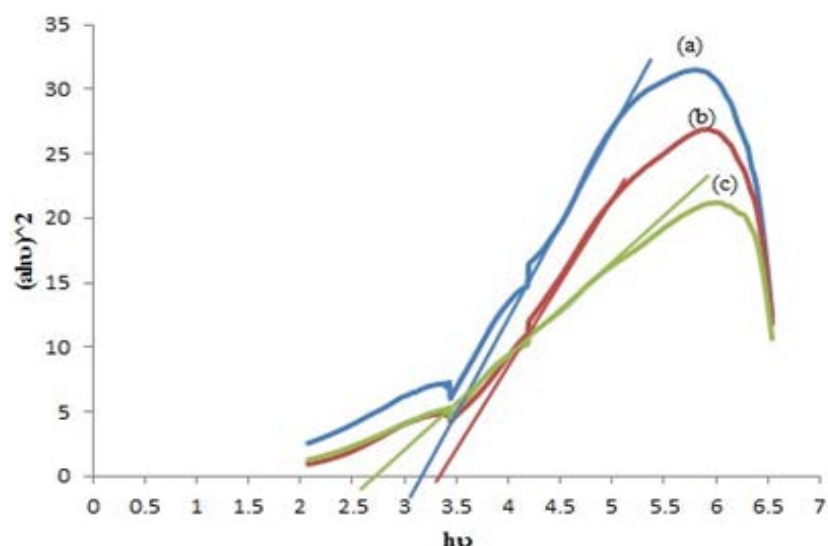Fig. 2. UV-Vis spectra of (a) $TiO_2$, (b) calcined CoZnAl-LDH/GO, and (c) graphene/CoZnAl MMO/$TiO_2$.



Fig. 3. Estimated band gap of (a) $TiO_2$, (b) calcined CoZnAl-LDH/GO, and (c) graphene/CoZnAl MMO/$TiO_2$.

GO and graphene/CoZnAl-MMO/$TiO_2$ were 3.3 and 2.7 eV, respectively. Therefore, it is clear that among $TiO_2$, calcined CoZnAl-LDH/GO, and graphene/CoZnAl-MMO/$TiO_2$, only the last one has photocatalytic activity in the visible light region.

Graphene/CoZnAl-MMO/$TiO_2$ scanning electron microscopy images (Fig. 4) show a uniform synthesis of the nanocomposite. The presence of graphene plates in the structure of the nanocomposite is quite clear (Fig. 4a). $TiO_2$ and CoZnAl-MMO nanoparticles are evenly distributed on the graphene plates (Fig. 4b). Fig. 5 represents the size distribution plot of the prepared Graphene/CoZnAl-MMO/$TiO_2$ particles, showing that most of the synthesized particles are in nano size. Commercial $TiO_2$-P25 nanoparticles can agglomerate, but the presence of graphene plates in the synthesized photocatalyst structure results in a flaky morphology that can reduce the agglomeration of the nanoparticles. The EDS analysis result of graphene/CoZnAl-MMO/$TiO_2$ photocatalyst is shown in Fig. 6. The peaks related to the metals and carbon of the nanocomposite structure confirm the successful synthesis of graphene/CoZnAl-MMO/$TiO_2$. Elemental mapping analysis of the synthesized nanoparticle is presented in Fig. 7. The results of this analysis show the uniform distribution of the elements in the nanoparticle structure, which is an evidence of its homogeneous and uniform synthesis.

The presence of graphene in the structure of the nanocomposite was investigated using FTIR analysis (Fig. 8) showing the C=C stretching vibration of graphene in 1,604 $cm^{-1}$. The broad band that appears in 3,410 $cm^{-1}$ is related to the O–H bond. Peaks appearing in the range of 400–1,000 $cm^{-1}$ are related to the stretching and bending
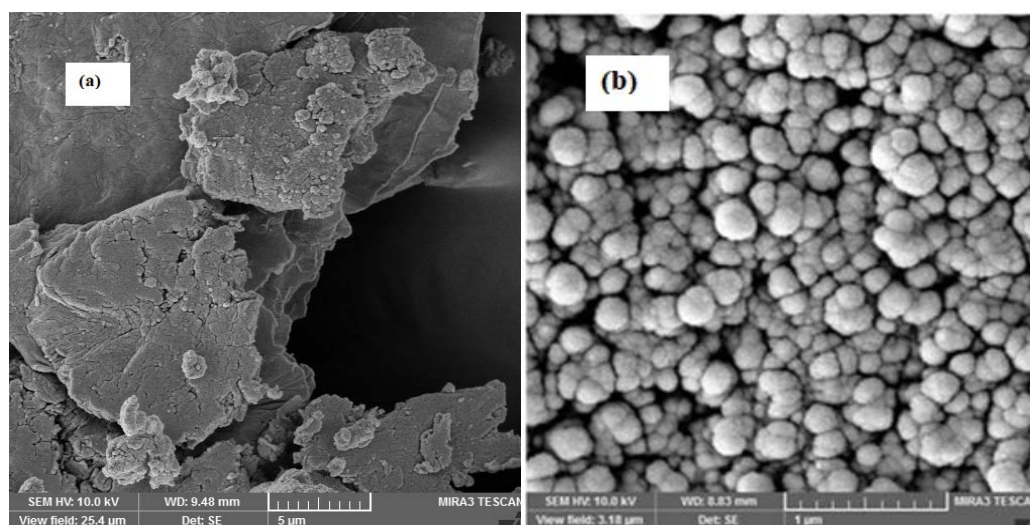
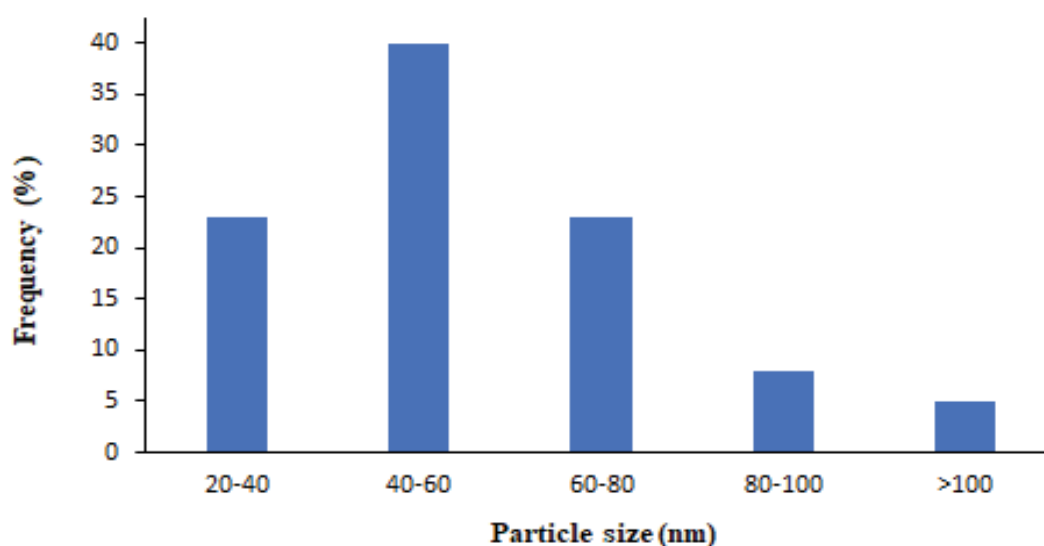Fig. 4. SEM images of graphene/CoZnAl-MMO/TiO$_2$ nanocomposite.



Fig. 5. Size distribution of the synthesized graphene/CoZnAl-MMO/TiO$_2$ nanocomposite.

vibrations of metal-oxygen bonds, which are related to metal oxides in the nanocomposite structure.

*3.2. Photocatalytic performance*

The influence of operating parameters (initial pH of the MB solution, MB concentration, and photocatalyst content) was investigated on removal efficiency. The obtained results are shown in Fig. 9. The pH of photocatalytic oxidation process affects its removal efficiency. The effect of the initial pH of the solution depends on the electrical charge of the contaminant and the pH$_{zpc}$ of the photocatalyst [23]. The pH$_{zpc}$ of graphene/CoZnAl-MMO/TiO$_2$ was obtained as 6.21 (Fig. 9a). MB is a cationic dye, as a result, the electrostatic interactions between the negatively charged photocatalyst surface and MB cations at pH values higher than pH$_{zpc}$ increase its adsorption and degradation. At pH values lower than pH$_{zpc}$, the photocatalyst surface is positively charged, resulting in MB repulsion and a decrease in MB adsorption efficiency [24] (Fig. 9b). Decolorization experiments were carried out at different pH values in the range of 4–9. For photocatalytic removal, pH = 6 showed the most adequate removal efficiency (Fig. 9c). An increase in the photocatalyst content resulted in higher MB removal efficiency due to the consequent rise of the number of active sites (Fig. 9d). According to Fig. 9e, changing the dye concentration in the range of 3–7 mg/L seemed to have no significant effect on its photocatalytic degradation.

The result of the present work was compared with those of similar published research works (Table 2), which shows that the result obtained in this work is acceptable considering the low-power visible-light source employed and the catalyst amount used.
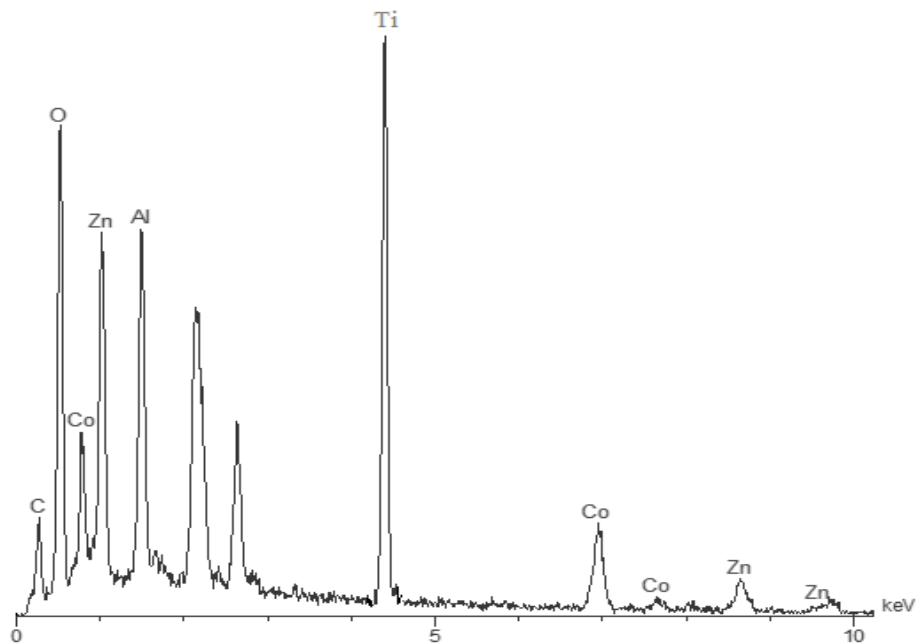
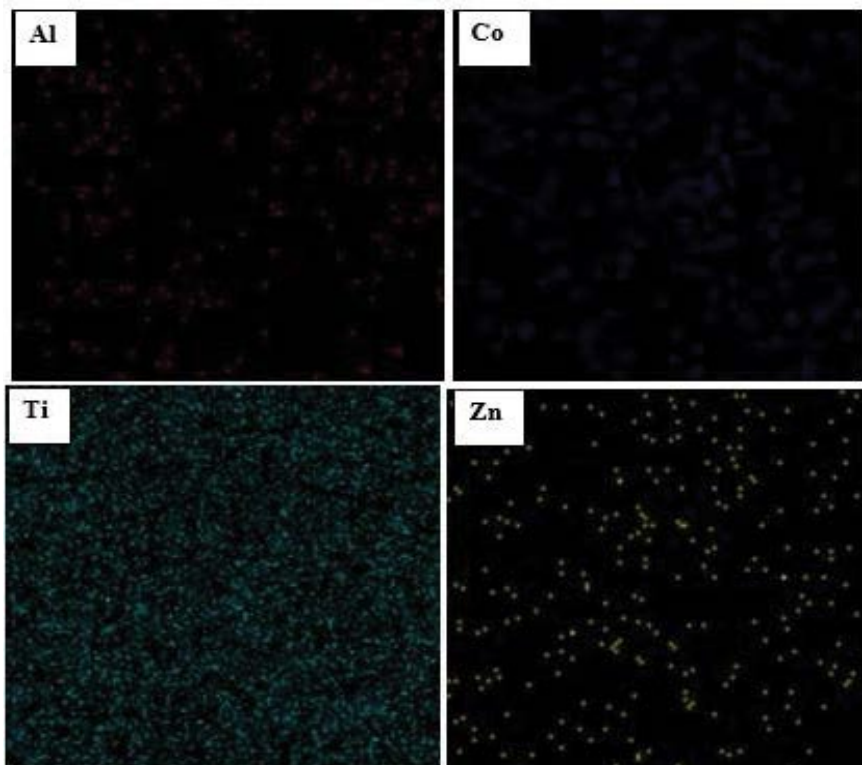Fig. 6. EDS results of graphene/CoZnAl-MMO/TiO$_2$ nanocomposite.



Fig. 7. Elemental mapping images of graphene/CoZnAl-MMO/TiO$_2$ nanocomposite.

### 3.3. Effect of different inhibitors

The contributions of hydroxyl radicals ($^\bullet$OH), super-oxide radical ions ($O_2^{\bullet-}$), and holes (h$^+$) were investigated in the photocatalytic MB degradation by graphene/CoZnAl-MMO/TiO$_2$ to understand the reaction mechanism [24]. A series of tests were performed in the presence of hydroquinone, sodium oxalate, and isopropanol, which are the inhibitors of $O_2^{\bullet-}$, h$^+$, and $^\bullet$OH, respectively. According to Fig. 10, the negative effect of various inhibitors on the
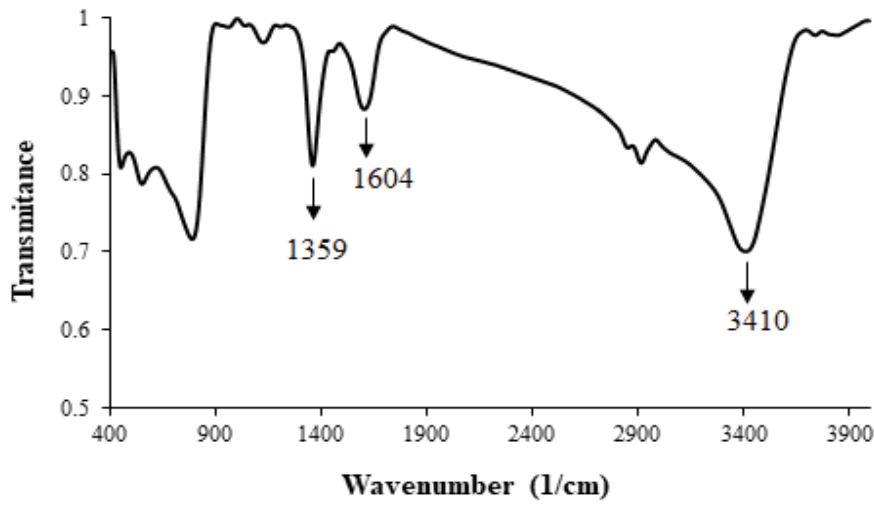
Fig. 8. FTIR spectra of graphene/CoZnAl-MMO/TiO$_2$ nanocomposite.

photocatalytic reaction efficiency is as follows: sodium oxalate < hydroquinone < isopropanol, confirming the superior role of hydroxyl radicals and holes in photocatalytic MB degradation by graphene/CoZnAl-MMO/TiO$_2$.

### 3.4. Kinetic modeling of the MB degradation process

The steps of MB photocatalytic degradation using graphene/CoZnAl-MMO/TiO$_2$ can be demonstrated by the following reactions [29]:

$$\text{Catalyst} + h\vartheta \xrightarrow{k_1} e^- + h^+ \tag{3}$$

$$e^- + h^+ \xrightarrow{k_2} \text{heat} \tag{4}$$

$$h^+ + H_2O \xrightarrow{k_3} OH^\bullet + H^+ \tag{5}$$

$$h^+ + OH^- \xrightarrow{k_4} OH^\bullet \tag{6}$$

$$OH^\bullet + e^- \xrightarrow{k_5} OH^- \tag{7}$$

$$OH^\bullet \xrightarrow{k_6} OH^- + h^+ \tag{8}$$

$$OH^\bullet + MB \xrightarrow{k_7} \text{Intermediate Product} \left(IP\right) \tag{9}$$

$$OH^\bullet + IP \xrightarrow{k_8} \text{Products}\left(P\right) \tag{10}$$

Based on reaction (9), the MB degradation rate can be written as follows:

$$\frac{-d\left[MB\right]}{dt} = k_7\left[OH^\bullet\right] \times \left[MB\right] \tag{11}$$

Based on reactions (3) to (10), the change of hydroxyl radical concentration during the dye degradation process can be written as follows:

$$\frac{d\left[OH^\bullet\right]}{dt} = k_3\left[H_2O\right] \times \left[h^+\right] + k_4\left[h^+\right] \times \left[OH^-\right]$$
$$- k_5\left[OH^\bullet\right] \times \left[e^-\right] - k_6\left[OH^\bullet\right]$$
$$- k_7\left[OH^\bullet\right] \times \left[MB\right] - k_8\left[OH^\bullet\right] \times \left[IP\right] \tag{12}$$

Based on the steady-state approximation of production and consumption of hydroxyl radicals, it can be assumed that the concentration of hydroxyl radicals is constant and does not change over time. Therefore, we consider the rate of hydroxyl radical concentration changes to be zero.

$$\frac{d\left[OH^\bullet\right]}{dt} = 0 \tag{13}$$

By applying the above assumption and considering the constant water concentration ($k_3$ [H$_2$O] = $k_3'$) the hydroxyl radical concentration can be written as follows:

$$\left[OH^\bullet\right] = \frac{k_3'\left[h^+\right] + k_4\left[h^+\right] \times \left[OH^-\right]}{k_5\left[e^-\right] + k_7\left[MB\right] + k_8\left[IP\right] + k_6} \tag{14}$$

Given Eqs. (3)–(6) and the equal concentrations of holes and electrons, the changes of [h$^+$] with respect to time can be written as:

$$\frac{d\left[h^+\right]}{dt} = k_1\left[\text{catalyst}\right] \times I - k_2\left[h^+\right]^2 - k_3\left[H_2O\right] \times \left[h^+\right]$$
$$- k_4\left[h^+\right] \times \left[OH^-\right] \tag{15}$$

where $I$ is the radiation intensity. According to Eqs. (5) and (6), the holes collide with hydroxide ions or water

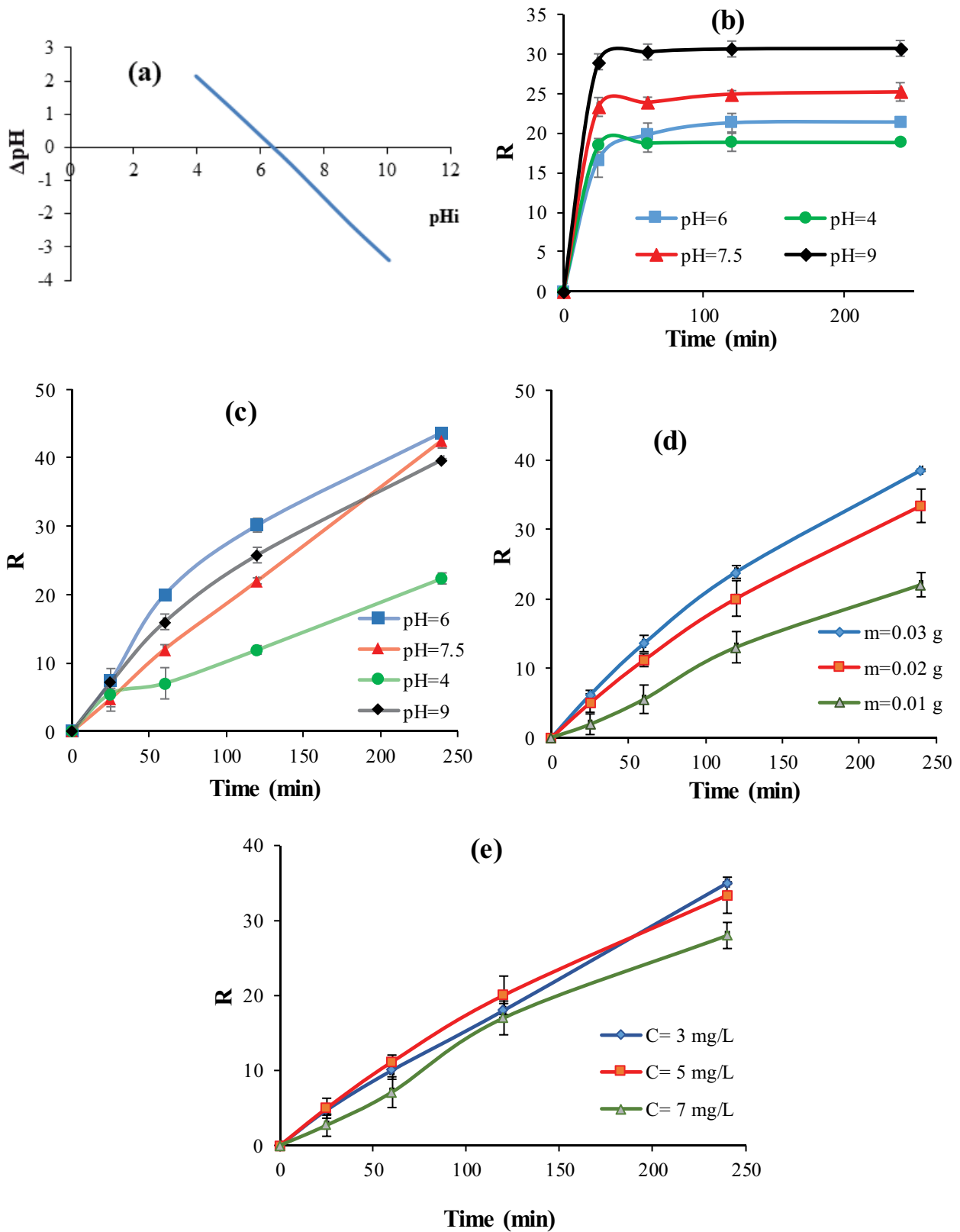Fig. 9. (a) Determination of $pH_{zpc}$ of graphene/CoZnAl-MMO/TiO$_2$ ([graphene/CoZnAl-MMO/TiO$_2$] = 5 g/L, [NaNO$_3$] = 0.1 mol/L, $T$ = 20°C, agitation rate = 150 rpm, $t$ = 24 h). (b) Effect of pH on MB adsorption. Effect of (c) pH, (d) catalyst dose, and (e) initial dye concentration on the photocatalytic degradation of MB. Constant operational conditions of experiments (b–e): [MB]$_0$ = 5 mg/L, [graphene/CoZnAl-MMO/TiO$_2$] = 0.4 g/L, pH = 6, $T$ = 28°C.

Table 2
Comparison of MB decolorization with different photocatalytic processes

| Catalyst | Light source | Concentration of MB (ppm) | Amount of catalyst | Time | References |
|---|---|---|---|---|---|
| $TiO_2$ mounted pumice | UV light (1.6 MW cm$^{-2}$) | 3 | 0.1 g | 48 h | [25] |
| $TiO_2$/ZrP | Solar radiation | 20 | 1 g/L | 4 h | [26] |
| $TiO_2$/MgAl-LDH | Hg UV lamp (100 W) | 13 | 1 g/L | 1 h | [27] |
| $SnO_2$/MgAl-LDH | Hg UV lamp (6 W) | 6 | 1 g/L | 1 h | [28] |
| ZnTi-LDH | Xenon lamp equipped with a wavelength filter (420 nm, 300 W) | 5 | 1 g/L | 100 min | [3] |
| Graphene/CoZnAl-MMO/$TiO_2$ | LED lamp (10 W) | 5 | 0.4 g/L | 4 h | This work |
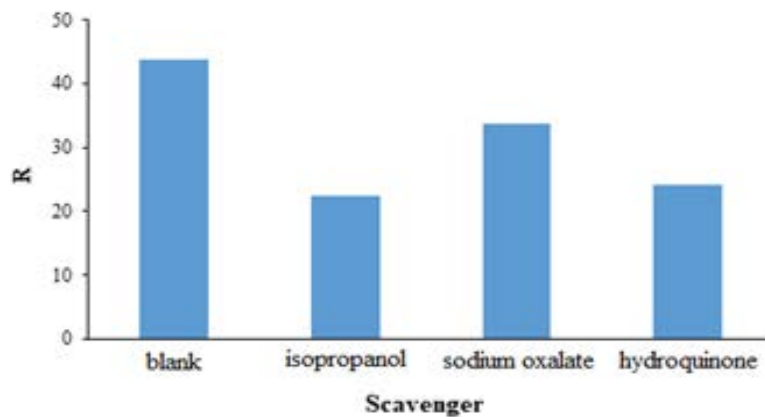


Fig. 10. The effect of different inhibitors on the photocatalytic MB degradation by graphene/CoZnAl-MMO/$TiO_2$ ([Catalyst] = 0.4 g/L, pH = 6, $T$ = 28°C, [MB]$_0$ = 5 mg/L, [Inhibitor] = 10 mM).

molecules to produce hydroxyl radicals. Due to the higher water concentration than hydroxide ion, especially at neutral pH region where the kinetic modeling experiments have been carried out, the expression $k_4[h^+] \times [OH^-]$ vs. $k_3[H_2O] \times [h^+]$ is negligible. Given the steady-state approximation for the holes, Eq. (15) is rewritten as Eq. (16).

$$k_1\left[\text{catalyst}\right] \times I = k_2\left[h^+\right]^2 - k_3'\left[h^+\right] \tag{16}$$

Two scenarios can be considered:

- The electron-hole recombination is faster than the reaction between the holes and the water molecules.
- The reaction rate between the holes and the water molecules is greater than the electron-cavity recombination rate.

In the first scenario, electron-hole recombination is very fast, in other words, the assumption $k_2[h^+]^2 \gg k_3'[h^+]$ is accepted [30]. In this case, the concentration of the holes is calculated as follows:

$$k_1\left[\text{catalyst}\right] \times I = k_2\left[h^+\right]^2 \tag{17}$$

$$\left[h^+\right]_1 = \left(\frac{k_1\left[\text{catalyst}\right]}{k_2}\right)^{1/2} \times I^{1/2} \tag{18}$$

In the second scenario, the rate of collision and reaction between the holes created in the valence band and the water molecules adsorbed by the catalyst surface is greater than the electron–hole recombination rate [31], so the hole concentration is calculated as follows:

$$k_1\left[\text{catalyst}\right] \times I = k_3'\left[h^+\right] \tag{19}$$

$$\left[h^+\right]_2 = \frac{k_1\left[\text{catalyst}\right]}{k_3'} \times I \tag{20}$$

Therefore, considering the two scenarios mentioned above and the placement of Eqs. (18) and (20) in Eq. (14), two equations for hydroxyl radical concentration and consequently, two equations for rate constant and two equations for reaction rate were obtained.

$$\left[OH^\bullet\right]_1 = \frac{k_3' \times \left(\dfrac{k_1\left[\text{catalyst}\right]}{k_2}\right)^{1/2} \times I^{1/2}}{k_5 \times \left(\dfrac{k_1\left[\text{catalyst}\right]}{k_2}\right)^{1/2} \times I^{1/2} + k_7\left[\text{MB}\right] + k_8\left[\text{IP}\right] + k_6} \tag{21}$$

Eq. (21) includes unknown [MB] and [IP] which are impossible to measure. But the following assumption can be met to simplify the equation.

$$[MB] + [IP] = [MB]_0 \tag{22}$$

where $[MB]_0$ is the initial dye concentration. The $k_7[MB] + k_8[IP]$ term is then rewritten as follows:

$$
\begin{aligned}
k_7[MB] + k_8[IP] &= k_7\left([MB]_0 - [IP]\right) + k_8\left([MB]_0 - [MB]\right) \\
&= (k_7 + k_8)[MB]_0 - k_7[IP] \\
&\quad - k_8[MB] \sim (k_7 + k_8)[MB]_0
\end{aligned}
\tag{23}
$$

According to Eq. (23), Eq. (21) is rewritten:

$$
[OH^\bullet]_1 = \frac{k_3' \times \left(\dfrac{k_1[\text{catalyst}]}{k_2}\right)^{1/2} \times I^{1/2}}{k_5 \times \left(\dfrac{k_1[\text{catalyst}]}{k_2}\right)^{1/2} \times I^{1/2} + (k_7 + k_8)[MB]_0 + k_6}
\tag{24}
$$

$$
[OH^\bullet]_1 = \frac{\dfrac{k_3'}{k_6} \times \left(\dfrac{k_1[\text{catalyst}]}{k_2}\right)^{1/2} \times I^{1/2}}{\dfrac{k_5}{k_6} \times \left(\dfrac{k_1[\text{catalyst}]}{k_2}\right)^{1/2} \times I^{1/2} + \left(\dfrac{k_7 + k_8}{k_6}\right)[MB]_0 + 1}
\tag{25}
$$

For the second scenario, with similar steps and assumptions to the first scenario, the equation of the hydroxyl radical concentration is written as follows:

$$
[OH^\bullet]_2 = \frac{\dfrac{k_1}{k_6} \times [\text{catalyst}] \times I}{\dfrac{k_5}{k_6} \times \left(\dfrac{k_1[\text{catalyst}]}{k_3'}\right) \times I + \left(\dfrac{k_7 + k_8}{k_6}\right)[MB]_0 + 1}
\tag{26}
$$

By placing Eqs. (25) and (26) in Eq. (11), two equations were obtained for the rate.

$$
r_1 = \frac{k_7 \times \dfrac{k_3'}{k_6} \times \left(\dfrac{k_1[\text{catalyst}]}{k_2}\right)^{1/2} \times I^{1/2}}{\dfrac{k_5}{k_6} \times \left(\dfrac{k_1[\text{catalyst}]}{k_2}\right)^{1/2} \times I^{1/2} + \left(\dfrac{k_7 + k_8}{k_6}\right)[MB]_0 + 1}[MB]
\tag{27}
$$

$$
r_2 = \frac{k_7 \times \dfrac{k_1}{k_6} \times [\text{catalyst}] \times I}{\dfrac{k_5}{k_6} \times \left(\dfrac{k_1[\text{catalyst}]}{k_3'}\right) \times I + \left(\dfrac{k_7 + k_8}{k_6}\right)[MB]_0 + 1}[MB]
\tag{28}
$$

By defining the constants α, β, and γ, the rate relations are simplified.

$$\alpha_1 = k_7 \times \frac{k_3'}{k_6} \times \left(\frac{k_1}{k_2}\right)^{1/2} \times I^{1/2} \tag{29}$$

$$\beta_1 = \frac{k_5}{k_6} \times \left(\frac{k_1}{k_2}\right)^{1/2} \times I^{1/2} \tag{30}$$

$$\gamma_1 = \frac{k_7 + k_8}{k_6} \tag{31}$$

$$r_1 = \frac{\alpha_1[\text{catalyst}]^{1/2}}{\beta_1[\text{catalyst}]^{1/2} + \gamma_1[MB]_0 + 1}[MB] \tag{32}$$

$$\alpha_2 = k_7 \times \frac{k_1}{k_6} \times I \tag{33}$$

$$\beta_2 = \frac{k_5}{k_6} \times \left(\frac{k_1}{k_3'}\right) \times I \tag{34}$$

$$\gamma_2 = \frac{k_7 + k_8}{k_6} \tag{35}$$

$$r_2 = \frac{\alpha_2[\text{catalyst}]}{\beta_2[\text{catalyst}] + \gamma_2[MB]_0 + 1}[MB] \tag{36}$$

By combining Eqs. (11), (32), and (36), the following equations were derived for the calculated rate constant values ($k_{cal}$).

$$k_{cal-1} = \frac{\alpha_1[\text{catalyst}]^{1/2}}{\beta_1[\text{catalyst}]^{1/2} + \gamma_1[MB]_0 + 1} \tag{37}$$

$$k_{cal-2} = \frac{\alpha_2[\text{catalyst}]}{\beta_2[\text{catalyst}] + \gamma_2[MB]_0 + 1} \tag{38}$$

Eqs. (37) and (38) were solved by employing the linear least squares method using the Solver program in the Excel software. To calculate the model error, the sum of squared error (SSE) and the root-mean-squared error (RMSE) were calculated based on the following equations.

$$SSE = \sum_{i=1}^{N} \left(y_{i,\text{cal}} - y_{i,\text{exp}}\right)^2 \tag{39}$$

$$RMSE = \sqrt{\frac{1}{N} \sum_{i=1}^{N} \left(y_{i,\text{cal}} - y_{i,\text{exp}}\right)^2} \tag{40}$$

Table 3
Constants, error (SSE, RMSE), and correlation coefficients ($R^2$) of the developed kinetic models

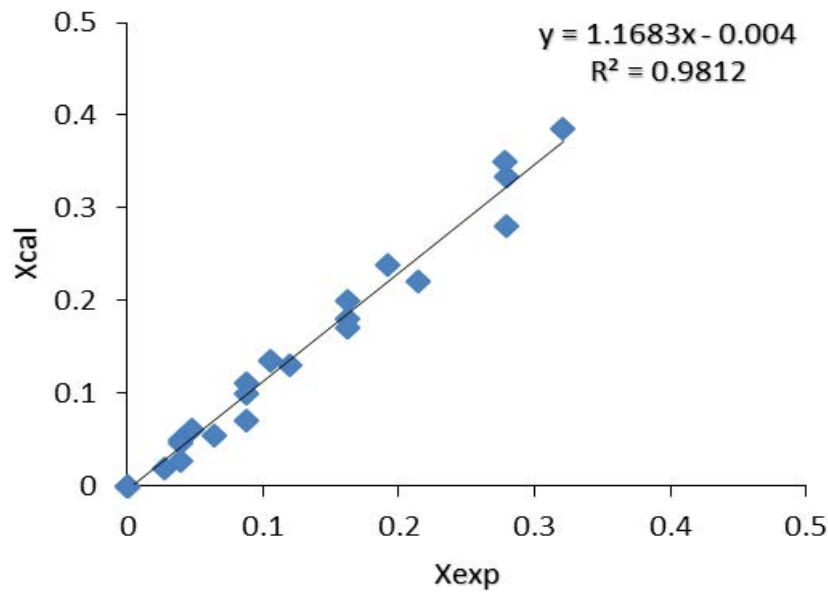| RMSE | SSE | $R^2$ | Constants values | Equation constant | Equation of $k_{cal}$ |
|---|---|---|---|---|---|
| $1.086 \times 10^{-3}$ | $2.36 \times 10^{-5}$ | 0.9907 | $3.9 \times 10^{-3}$ | $\alpha_1 = k_7 \times \dfrac{k'_3}{k_6} \times \left(\dfrac{k_1}{k_2}\right)^{1/2} \times I^{1/2}$ | $k_{cal-1} = \dfrac{\alpha_1 \left[\text{catalyst}\right]^{1/2}}{\beta_1 \left[\text{catalyst}\right]^{1/2} + \gamma_1 \left[\text{MB}\right]_0 + 1}$ |
| | | | 1.2146 | $\beta_1 = \dfrac{k_5}{k_6} \times \left(\dfrac{k_1}{k_2}\right)^{1/2} \times I^{1/2}$ | |
| | | | 1.7854 | $\gamma_1 = \dfrac{k_7 + k_8}{k_6}$ | |
| $4.261 \times 10^{-3}$ | $3.63 \times 10^{-4}$ | 0.8411 | 185.5096 | $\alpha_2 = k_7 \times \dfrac{k_1}{k_6} \times I$ | $k_{cal-2} = \dfrac{\alpha_2 \left[\text{catalyst}\right]}{\beta_2 \left[\text{catalyst}\right] + \gamma_2 \left[\text{MB}\right]_0 + 1}$ |
| | | | 1,454,025 | $\beta_2 = \dfrac{k_5}{k_6} \times \left(\dfrac{k_1}{k'_3}\right) \times I$ | |
| | | | 32,121.56 | $\gamma_2 = \dfrac{k_7 + k_8}{k_6}$ | |



Fig. 11. Comparison of the experimental conversion fractions and those calculated by the developed kinetic model.

where $N$ is the number of data points and $y_{i,\text{pred}}$ and $y_{i,\text{exp}}$ are the predicted and experimental removal efficiencies, respectively. The results shown in Table 3 prove that the predicted kinetic model based on the assumption of high electron–hole recombination rate fits the experimental data more adequately.

Finally, by placing Eq. (37) in Eq. (39), the conversion fraction was obtained as follows:

$$X = 1 - \exp\left(-k_{cal-1}t\right) \tag{41}$$

Fig. 11 illustrates the relationship between the $X_{cal}$ and the $X_{exp}$ values. As can be seen, the data obtained from the

kinetic model are in good agreement with the experimental data. This proves that the proposed model for the photocatalytic degradation of MB by graphene/CoZnAl-MMO/TiO$_2$ works well and can predict MB conversion fraction at the studied conditions.

## 4. Conclusion

A new photocatalyst graphene/CoZnAl-MMO/TiO$_2$ was synthesized. The addition of graphene and MMO to the nanocomposite reduced the band gap and caused the photocatalytic activity of graphene/CoZnAl-MMO/TiO$_2$ in the visible area. The photocatalyst was used to decolorize the MB solution. According to the results, the best

removal conditions were obtained at pH = 6, [MB] = 5 mg/L and [catalyst] = 0.4 g/L. According to the obtained $R^2$, SSE, and RMSE values, the values obtained for the calculated and experimental rate constants were in good agreement. The conversion fractions obtained from the pseudo-first-order equation using experimental and calculated rate constants had good agreement as well.

## Acknowledgments

## References

[1] H.S. Jung, Y.J. Hong, Y. Li, J. Cho, Y.-J. Kim, G.-C. Yi, Photocatalysis using GaN nanowires, ACS Nano, 2 (2008) 637–642.

[2] G. Saupe, Y. Zhao, J. Bang, N. Yesu, G. Carballo, R. Ordonez, T. Bubphamala, Evaluation of a new porous titanium-niobium mixed oxide for photocatalytic water decontamination, Microchem. J., 81 (2005) 156–162.

[3] M. Shao, J. Han, M. Wei, D.G. Evans, X. Duan, The synthesis of hierarchical Zn–Ti layered double hydroxide for efficient visible-light photocatalysis, Chem. Eng. J., 168 (2011) 519–524.

[4] M. Rauf, M. Meetani, S. Hisaindee, An overview on the photocatalytic degradation of azo dyes in the presence of $TiO_2$ doped with selective transition metals, Desalination, 276 (2011) 13–27.

[5] R. Acharya, B. Naik, K. Parida, Cr(VI) remediation from aqueous environment through modified-$TiO_2$-mediated photocatalytic reduction, Beilstein J. Nanotechnol., 9 (2018) 1448–1470.

[6] H. Wang, X. Yuan, Y. Wu, H. Huang, X. Peng, G. Zeng, H. Zhong, J. Liang, M. Ren, Graphene-based materials: fabrication, characterization and application for the decontamination of wastewater and wastegas and hydrogen storage/generation, Adv. Colloid Interface Sci., 195 (2013) 19–40.

[7] H. Li, Q. Deng, J. Liu, W. Hou, N. Du, R. Zhang, X. Tao, Synthesis, characterization and enhanced visible light photocatalytic activity of $Bi_2MoO_6$/Zn–Al layered double hydroxide hierarchical heterostructures, Catal. Sci. Technol., 4 (2014) 1028–1037.

[8] M. Sharifi-Bonab, S. Aber, D. Salari, F. Khodam, Water treatment with CoZnAl-LDH and its mixed metal oxide, Water Pract. Technol., 16 (2021) 1386–1396.

[9] L. Mohapatra, K. Parida, Zn–Cr layered double hydroxide: visible light responsive photocatalyst for photocatalytic degradation of organic pollutants, Sep. Purif. Technol., 91 (2012) 73–80.

[10] M.A. Djebbi, M. Braiek, P. Namour, A.B.H. Amara, N. Jaffrezic-Renault, Layered double hydroxide materials coated carbon electrode: new challenge to future electrochemical power devices, Appl. Surf. Sci., 386 (2016) 352–363.

[11] M.S. Mostafa, A.-S.A. Bakr, A.M. El Naggar, E.-S.A. Sultan, Water decontamination via the removal of Pb(II) using a new generation of highly energetic surface nano-material: $Co^{+2}Mo^{+6}$ LDH, J. Colloid Interface Sci., 461 (2016) 261–272.

[12] S. Berner, P. Araya, J. Govan, H. Palza, Cu/Al and Cu/Cr based layered double hydroxide nanoparticles as adsorption materials for water treatment, J. Ind. Eng. Chem., 59 (2018) 134–140.

[13] Š. Paušová, J. Krýsa, J. Jirkovský, G. Mailhot, V. Prevot, Photocatalytic behavior of nanosized $TiO_2$ immobilized on layered double hydroxides by delamination/restacking process, Environ. Sci. Pollut. Res., 19 (2012) 3709–3718.

[14] S. Kumar, M.A. Isaacs, R. Trofimovaite, L. Durndell, C.M. Parlett, R.E. Douthwaite, B. Coulson, M.C. Cockett, K. Wilson, A.F. Lee, P25@CoAl layered double hydroxide heterojunction nanocomposites for $CO_2$ photocatalytic reduction, Appl. Catal., B, 209 (2017) 394–404.

[15] M. Sharifi-Bonab, S. Aber, D. Salari, F. Khodam, Synthesis of CoZnAl-layered double hydroxide/graphene oxide

[16] nanocomposite for the removal of methylene blue: kinetic, thermodynamic, and isotherm studies, Environ. Prog. Sustainable Energy, 39 (2020) e13316.

[16] J.L. Gunjakar, T.W. Kim, H.N. Kim, I.Y. Kim, S.-J. Hwang, Mesoporous layer-by-layer ordered nanohybrids of layered double hydroxide and layered metal oxide: highly active visible light photocatalysts with improved chemical stability, J. Am. Chem. Soc., 133 (2011) 14998–15007.

[17] D.D.W. Rufuss, S. Iniyan, L. Suganthi, P. Davies, Low mass fraction impregnation with graphene oxide (GO) enhances thermo-physical properties of paraffin for heat storage applications, Thermochim. Acta, 655 (2017) 226–233.

[18] J. Xu, S. Gai, F. He, N. Niu, P. Gao, Y. Chen, P. Yang, Reduced graphene oxide/$Ni_{1-x}Co_x$Al-layered double hydroxide composites: preparation and high supercapacitor performance, Dalton Trans., 43 (2014) 11667–11675.

[19] B. Li, Y. Zhao, S. Zhang, W. Gao, M. Wei, Visible-light-responsive photocatalysts toward water oxidation based on NiTi-layered double hydroxide/reduced graphene oxide composite materials, ACS Appl. Mater. Interfaces, 5 (2013) 10233–10239.

[20] S. Mahalingam, J. Ramasamy, Y.-H. Ahn, Synthesis and application of graphene-$\alpha MoO_3$ nanocomposite for improving visible light irradiated photocatalytic decolorization of methylene blue dye, J. Taiwan Inst. Chem. Eng., 80 (2017) 276–285.

[21] K. Klemkaite, I. Prosycevas, R. Taraskevicius, A. Khinsky, A. Kareiva, Synthesis and characterization of layered double hydroxides with different cations (Mg, Co, Ni, Al), decomposition and reformation of mixed metal oxides to layered structures, Cent. Eur. J. Chem., 9 (2011) 275–282.

[22] E. Davis, N. Mott, Conduction in non-crystalline systems V. Conductivity, optical absorption and photoconductivity in amorphous semiconductors, Philos. Mag., 22 (1970) 903–922.

[23] J. Xia, A. Wang, X. Liu, Z. Su, Preparation and characterization of bifunctional, $Fe_3O_4$/ZnO nanocomposites and their use as photocatalysts, Appl. Surf. Sci., 257 (2011) 9724–9732.

[24] A.N. Shafawi, R.A. Mahmud, K.A. Ali, L.K. Putri, N.I.M. Rosli, A.R. Mohamed, $Bi_2O_3$ particles decorated on porous g-$C_3N_4$ sheets: enhanced photocatalytic activity through a direct Z-scheme mechanism for degradation of Reactive Black 5 under UV–Vis light, J. Photochem. Photobiol., A, 389 (2020) 112289, doi: 10.1016/j.jphotochem.2019.112289.

[25] X.-Y. Chuan, M. Hirano, M. Inagaki, Preparation and photocatalytic performance of anatase-mounted natural porous silica, pumice, by hydrolysis under hydrothermal conditions, Appl. Catal., B, 51 (2004) 255–260.

[26] S. Gokulakrishnan, P. Parakh, H. Prakash, Degradation of Malachite green by potassium persulphate, its enhancement by 1,8-dimethyl-1,3,6,8,10,13-hexaazacyclotetradecane nickel(II) perchlorate complex, and removal of antibacterial activity, J. Hazard. Mater., 213 (2012) 19–27.

[27] E. Seftel, E. Popovici, E. Beyers, M. Mertens, H. Zhu, E. Vansant, P. Cool, New $TiO_2$/MgAl-LDH nanocomposites for the photocatalytic degradation of dyes, J. Nanosci. Nanotechnol., 10 (2010) 8227–8233.

[28] E. Dvininov, M. Ignat, P. Barvinschi, M. Smithers, E. Popovici, New $SnO_2$/MgAl-layered double hydroxide composites as photocatalysts for cationic dyes bleaching, J. Hazard. Mater., 177 (2010) 150–158.

[29] A. Amani-Ghadim, M.S. Dorraji, Modeling of photocatalyatic process on synthesized ZnO nanoparticles: kinetic model development and artificial neural networks, Appl. Catal., B, 163 (2015) 539–546.

[30] Y. Li, S. Sun, M. Ma, Y. Ouyang, W. Yan, Kinetic study and model of the photocatalytic degradation of rhodamine B (RhB) by a $TiO_2$-coated activated carbon catalyst: effects of initial RhB content, light intensity and $TiO_2$ content in the catalyst, Chem. Eng. J., 142 (2008) 147–155.

[31] A. Khataee, M. Fathinia, S. Aber, Kinetic study of photocatalytic decolorization of CI Basic Blue 3 solution on immobilized titanium dioxide nanoparticles, Chem. Eng. Res. Des., 89 (2011) 2110–2116.